Lab on a Chip

PAPER

View Article Online
View Journal | View Issue

Cite this: *Lab Chip*, 2017, **17**, 4059

Enhanced surface acoustic wave cell sorting by 3D microfluidic-chip design

W. L. Ung, [a] K. Mutafopulos, [a] P. Spink, [a] R. W. Rambach,[b] T. Franke *[b] and D. A. Weitz [ac]

Received 9th July 2017,
Accepted 3rd October 2017

DOI: 10.1039/c7lc00715a

rsc.li/loc

We demonstrate an acoustic wave driven microfluidic cell sorter that combines advantages of multilayer device fabrication with planar surface acoustic wave excitation. We harness the strong vertical component of the refracted acoustic wave to enhance cell actuation by using an asymmetric flow field to increase cell deflection. Precise control of the 3-dimensional flow is realized by topographical structures implemented on the top of the microchannel. We experimentally quantify the effect of the structure dimensions and acoustic parameter. The design attains cell sorting rates and purities approaching those of state of the art fluorescence-activated cell sorters with all the advantages of microfluidic cell sorting.

Introduction

Fluorescence-activated cell sorting (FACS) is a method for extracting desired cells based on their biological characteristics.[1] These characteristics are distinguished using fluorescence-based assays. A sheath flow focuses cells to a narrow stream, accelerating cells to high velocity and separating them along the direction of flow. This stream must be aligned with the optics of the instrument to make accurate measurements. To sort cells, the fluid stream is broken into droplets that contain single cells. Droplets containing target cells are selectively charged and subsequently deflected in an electric field. The entire process occurs rapidly enough for FACS instruments to operate at rates as high as tens of kHz, while still retaining high purity.[1,2] However, FACS also suffers from several limitations of the technique: the large volumes of sheath fluid required to reach high velocities make it difficult to sort small numbers of cells;[3] moreover, the droplet aerosol produced during sorting poses a potential biohazard when using infectious cells.[1,4,5] One way to overcome these limitations is to use microfluidic devices composed of microscale flow channels that can handle minute volumes of fluid in a closed device without producing drops.[6,7] The small volume of each microfluidic device reduces the dead volume of the system and minimizes the loss of sample. Alignment of microfluidic devices is simplified because the flow channels are embedded reproducibly within each device; moreover, cross contamination between different samples can be eliminated by replacing the device, rather than cleaning it. Furthermore, microfluidic devices can sort cells without producing aerosols, alleviating the potential risks associated with sorting hazardous samples.[8–10] Microfluidic cell sorters implement a variety of actuation mechanisms, such as piezoelectric actuation,[11] dielectrophoresis of droplets,[10,12,13] optical manipulation such as pulsed laser induced cavitation,[9,14] and surface acoustic wave (SAW) deflection.[8,15,16] In spite of the benefits of microfluidic devices for cell sorting, they are not widely used because microfluidic devices cannot match the speed of FACS instruments; to become widely used, microfluidic devices must be able to sort at higher rates.[5] Surface acoustic waves have the potential to reach high rates, offering a robust and contactless microfluidic method for sorting cells by sound using high speed electronics.[17] Devices exciting standing acoustic waves have been used to dynamically pattern the acoustic field within the microchannel to achieve fine control over each cell's spatial position,[15,16,18–21] but they have yet to reach rates comparable to FACS, when used to perform the sorting. In SAW devices using standing waves the acoustic wavelength determines the pressure node spacing that is used to separate the cells and that is therefore fixed for a desired node spacing. Traveling SAW devices can be operated at different frequencies without changing the device design, enabling the use of increasing frequencies to increase the acoustic force exploited for sorting without changing the device design,[22] and therefore are promising and versatile candidates for high speed microfluidic sorting even though yet they do not reach FACS rates. However, if these devices could be improved by developing a more efficient way to exploit the

[a] *School of Engineering and Applied Sciences, Harvard University, Cambridge, MA, 02138, USA*
[b] *Biomedical Engineering, School of Engineering, University of Glasgow, Glasgow, G12 8QQ, UK. E-mail: Thomas.Franke@glasgow.ac.uk*
[c] *Department of Physics, Harvard University, Cambridge, MA, 02138, USA*

sound pulse for deflection, traveling SAW devices would be more widely adopted for cell sorting applications.

Here, we demonstrate a microfluidic cell sorter based on traveling SAW actuation that screens and sorts cells at rates approaching those of commercial FACS instruments. The device contains multi-layer features that enhance the capabilities of a SAW sorter by harnessing the component of the acoustic wave oriented normal to the plane of the substrate. The multi-layer features consist of a three-dimensional flow-focusing nozzle and a slanted ceiling groove, which guides cells to the retention outlet following SAW deflection. We find operating conditions which yield efficient sorting in this device, and sort fluorescently-labelled cells from mixed samples. The device achieves sorting at a rate of 9000 events per s with 60% purity and yields of 92% purity, while operating at 1000 events per s; this level of performance approaches that of a FACS instrument operating in its high-purity mode.

Results and discussion

A SAW that impinge on the interface of a fluid in a microfluidic device, refracts and establishes longitudinal acoustic waves in the fluid, as shown in Fig. 1a.[23] The angle of refraction for SAWs is known as the Rayleigh angle, θ_R, and depends on the speed of sound in the liquid, v_l, and the speed of the SAW on the substrate, v_s, according to Snell's law, $\sin\theta_R = v_l/v_s$.[23,24] The refracted acoustic wave exerts forces aligned with the direction of wave propagation on cells flowing through the microfluidic device.[7,17,22,24,25] Because the SAW travels along the lithium niobate surface several times faster than the acoustic wave in the liquid,[26] the refracted wave is largely aligned with the substrate's surface normal.[27] The device is oriented such that the refracted wave pushes cells mainly upward in the vertical, or $+z$, direction. We present a device that sorts cells based on their vertical deflection actuated by the refracted acoustic wave. We could not observe the formation of standing acoustic waves caused by the acoustic reflection at channel walls as has been reported elsewhere,[28–30] probably of the small impedance mismatch of the fluid and PDMS material and the channel dimensions. We also did not observe any near field effect such as streaming roll as has been reported in Devendran *et al.*,[31] or acoustic interference patterns[32] because of the short pulse length and the comparatively large size of the cells. The proposed design enhances sorting performance, because it harnesses a larger proportion of the power carried by the SAW. We achieve this by a 3-dimensional design of the microfluidic channel.

In our design, the microfluidic device is bonded directly onto a lithium niobate substrate adjacent to an interdigital transducer (IDT). When a RF signal is applied, the IDT generates travelling SAWs. Acoustic waves are excited in the channel adjacent to the IDT, in what is referred to as the sorting region of the device. Cells enter the sorting region of the device through the vertical flow-focusing nozzle. A slanted groove extends above the sorting region and enhances the deflection of cells by acoustic waves. Immediately after the sorting region, the device's main channel bifurcates: each cell

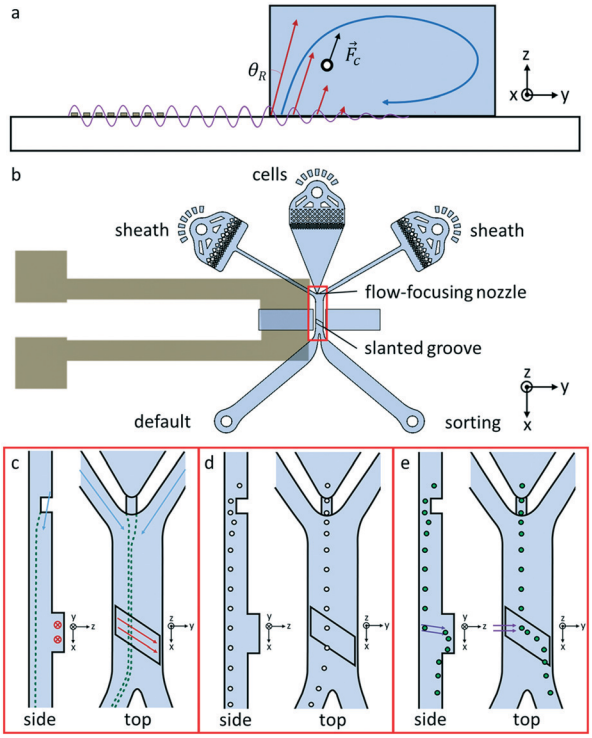

Fig. 1 A multi-layer design for cell sorting with surface acoustic waves (a) a cross-section of the device is shown to illustrate the refraction of surface acoustic waves. The interdigital transducer (gold) generates a surface acoustic wave (purple). The surface acoustic wave travels along the substrate surface (white rectangle) in the $+y$ direction. The surface acoustic wave refracts, upon contact with the fluid (light blue) within the microfluidic device, forming a longitudinal acoustic wave (red arrows) in the liquid. Refraction occurs at a small Rayleigh angle, θ_R. The refracted acoustic wave exerts an acoustic radiation pressure on the cells (white circle) as well as driving fluid flow by acoustic streaming (blue arrow). (b) The design developed for cell sorting using surface acoustic waves is illustrated. The flow channel of the microfluidic device (blue) is positioned next to the interdigital transducer (IDT). The flow channel has a cell inlet and two sheath inlets through which the sample and sheath flows for flow focusing are injected respectively. The cell phase flow and sheath flows meet at the vertical flow-focusing nozzle; cells flow through the vertical flow-focusing nozzle into the sorting region of the device (red rectangle). Cells are probed by the optical system and a sorting pulse is applied, when a target cell is detected. Desired cells are sorted using acoustic waves and are deflected to leave the sorting region through the sorting outlet, while the rest of the cells pass through the sorting region unperturbed *via* the default outlet. (c) After the flow focusing nozzle, sheath flows (blue arrows) confine the flow from the cell inlet (green dashed line) into a narrow thread at the bottom of the channel. At the top of the channel, the flow is pulled across the channel by the slanted groove (red arrows). The fluid within the groove flows along the groove's long axis, but the flow of liquid at the bottom of the channel is largely unperturbed. (d) Cells lacking the desired characteristics (white circles) are not sorted and exit the device through the waste outlet without interacting with the flow within the groove. (e) If a target cell (green circles) is detected, surface acoustic waves are applied (purple arrows). They refract into the device and deflect the cell into the groove, where it is carried by the flow within the groove across the channel and out of the device through the retention outlet.

either flows directly into the default outlet or acoustic waves actuate the cell into the sorting outlet. The positions of the distinct features of the sorting device with respect to the IDT are shown in Fig. 1b.

The design uses multi-layer features to create flows with vertical components. The vertical flow-focusing nozzle is a multi-layer feature formed at the intersection of the cell phase inlet with the channels containing the sheath flow. The cell inlet channel has a vertical constriction just prior to where it converges with the sheath channels, so the sheath flows focus the cell sample phase laterally and downward into a narrow thread at the bottom of the channel.[33] This ensures that all cells flow along the bottom of the channel and are confined into a small region initially. If cells manage to reach the top of the channel by acoustic deflection, they interact with a different multi-layer feature, the slanted ceiling groove. The slanted groove channels fluid along the groove, setting up a flow that carries cells laterally across the sorting region of the device. The magnitude of the lateral flow decreases with distance from the groove,[34] and it is negligible at the bottom of the channel. The flows created by the multi-layer features of the device are illustrated in Fig. 1c. Cells can thus be sorted based on their vertical position, because the flow in the groove directs cells at different heights into different outlets.

The vertical position of cells can be set by triggered acoustic wave actuation. In the absence of acoustic waves, cells transit directly through the sorting region of the device and leave through the default outlet without interacting with the slanted groove, as shown in Fig. 1d. However, an acoustic wave pulse can deflect target cells, using the refracted wave to selectively push cells vertically to the top of the sorting channel. At the top of the channel, the flow within the slanted groove guides these cells laterally across the sorting channel and into the sorting outlet, as shown in Fig. 1e. The experimentally observed cell tracks captured during device operation verify that cells follow these expected trajectories with and without acoustic wave actuation, as illustrated in Fig. 2a and b respectively. Although cells are still deflected without a slanted groove, the lateral displacement is much smaller as compared to deflection with the groove, as depicted in the cell track shown in Fig. 2c. Thus, the slanted groove only interacts with cells deflected by the refracted wave converting their vertical motion into lateral motion that can be used to segregate cells.

To quantify the sorting success and to optimize devices with slanted grooves, we measure the sorting performance using the tracks of moving cells. When a pulse of acoustic waves is applied to a cell, we use a high-speed camera to record the corresponding cell track; we combine the results from several cell tracks to determine a sorting success rate. If we increase the power carried by the acoustic wave, we can increase the sorting success rate. For every condition we test, we measure how much power is required to exceed a 90% success rate and define this as the threshold power. Moreover, if we operate in a regime where the power required is

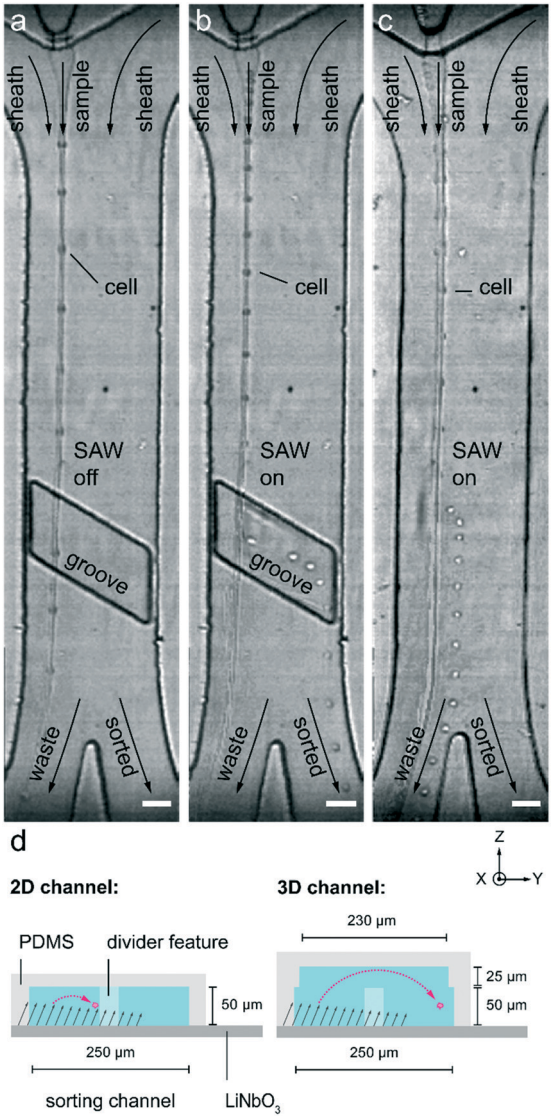

Fig. 2 The slanted groove enhances cell deflection using surface acoustic waves. Fast camera movies are captured as cells flow through the sorting region of the slanted groove device. Multiple frames from a single cell transit event are superimposed to create an image depicting the trajectory of a cell passing through the device (flow direction from top to bottom). (a) When no pulse is applied, the cell follows straight along the same trajectory as the bulk of the cell phase fluid. The cell passes through the sorting region and underneath the slanted groove without deflection and exits the device through the default outlet (waste outlet). (b) When a cell is detected, a radio frequency signal of 38.26 dBm is applied for 100 μs to generate a surface acoustic wave pulse. In the device with a slanted groove, the refracted acoustic wave deflects the cell into the slanted groove, where it is carried across the sorting region of the channel by the flow of sheath fluid within the groove. The sorted cell moves laterally more than 150 μm and exits the device through the sorting outlet. (c) For devices without a slanted groove, the sorted cell is still deflected by the acoustic wave, but the cell is only displaced about 50 μm laterally under the same acoustic conditions. In all cases, the cell phase fluid is visible as a dark thread in the images, because of the index of refraction difference between the sheath fluid, phosphate-buffered saline, and the cell phase containing Optiprep. The cell tracks depicted here are projections of about 20 frames measured with a high-speed camera at 11 267 fps. The scale bars correspond to 50 μm. (d) Cross sectional view of the microchannels in (c).

below the threshold power, we expect better sorting performance. We observe how cell velocity and acoustic wave pulse length affect the sorting performance to determine the screening rate these devices can achieve. We also measure how well different types of cells can be sorted. In addition, we want to understand how the geometry of the groove impacts sorting performance. For these devices, the parameters are coupled, so we vary one parameter at a time to understand the overall behaviour of the device. To ensure that results are reproducible, the threshold power is determined on three different days and with at least 48 individual experiments that are evaluated and averaged as shown in Fig. 2 and 3. The threshold power was tested against flow rate, pulse length, groove width, and groove height as shown in Fig. 3 to determine the ideal threshold power. We aim to find settings that can yield sorting at high event rates by choosing a high cell velocity and a low pulse length; however, we keep the sorting success high using groove dimensions that enable sorting at low power levels and exceeding the threshold power.

Dependence on flow velocity

The velocity at which cells transit through the sorting region of the device limits the screening rate of the device because it effects the exposure time of the cell to the acoustics. Moreover, if a cell is still in the sorting region of the device when the next cell enters the region of deflection, the two cells cannot be sorted independently. To prevent this, cells must transit quickly through the sorting region of the device. We vary the total flow rate to control the average cell velocity and determine its effect on the sorting process. At low flow rates,

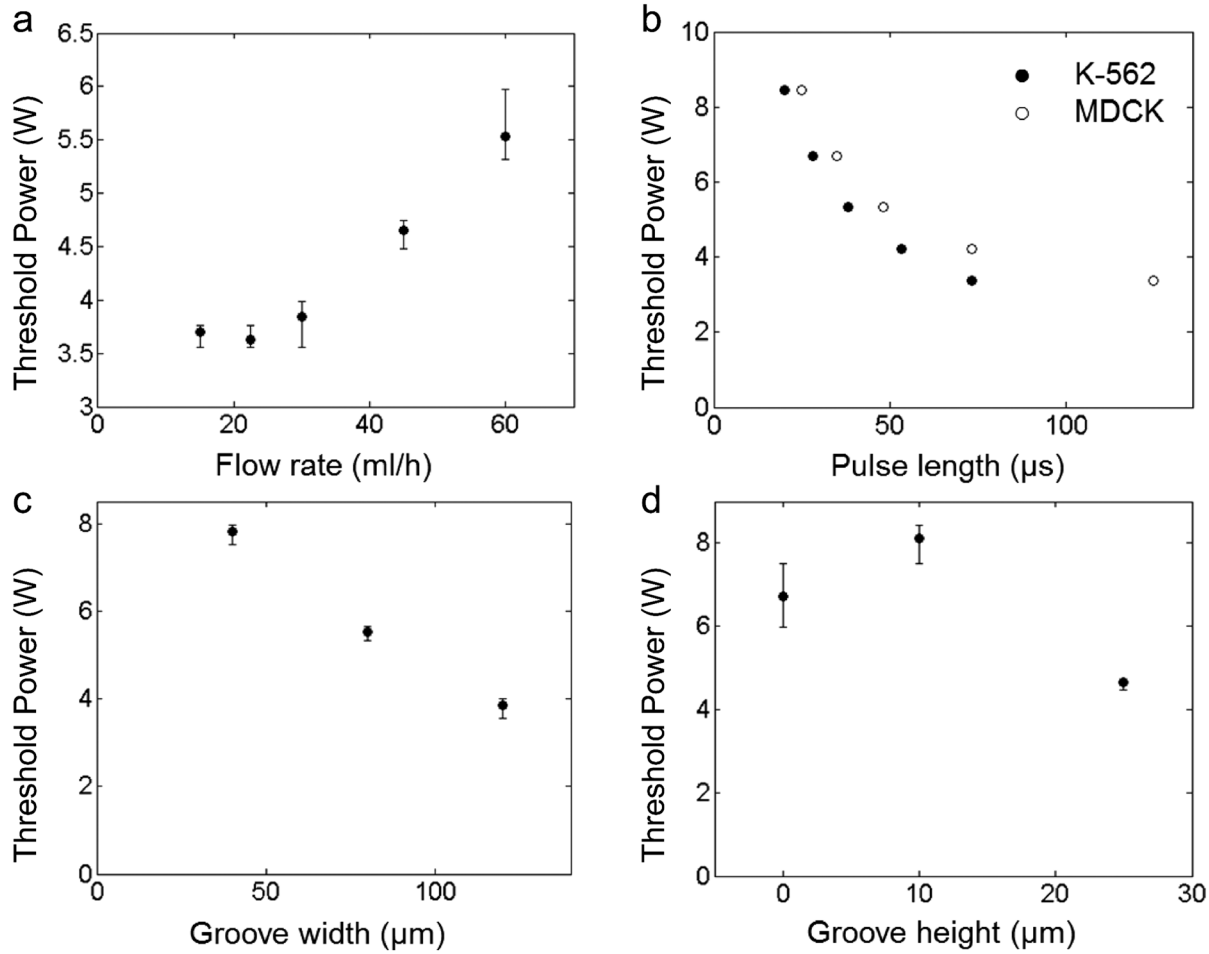

Fig. 3 Cell sorting performance of groove-enhanced devices. Sorting devices with slanted grooves reliably actuate cells for a wide range of operating conditions. The symbols on each plot are centered on the mean of the three independent threshold values, while the error bars depict the full range of threshold values. For points without visible error bars, the marker size exceeds the extent of the error bars. We only varied one parameter at a time and kept the other parameters constant. We used a groove width of 120 μm, a height of 25 μm, flow rate of 45.5 ml h^{-1} and a pulse length of 50 μs. (a) As the flow rate is varied, the threshold power required for sorting increases, except at the lower range of flow rates, where it appears there is a minimum amount of power necessary for sorting. (b) As the applied radio frequency power is increased, the length of the pulse necessary to deflect a given cell type decreases. The device actuates both, adherent Madin-Darby canine kidney cells (MDCK; open symbols, ○) and non-adherent chronic myelogenous leukemia cells (K-562; filled symbols, ●) with performance levels sufficient to achieve high speed cell sorting. (c) The threshold power decreases linearly as the groove is widened. (d) The threshold power changes non-monotonically as the groove height is increased, but sorting with the lowest required power is achieved for the deepest tested grooves.

the threshold power is essentially uncorrelated with the applied flow rate, but at higher flow rates, there appears to be a direct correlation between threshold power and applied flow rate, as the cell deflection becomes limited by its exposure to the acoustic wave pulse. The relationship between the threshold power of the SAW pulse and the overall device flow rate is depicted in Fig. 3a. The results show that cells can be deflected consistently even at high flow rates of 60 ml h^{-1}.

Dependence on pulse length

The minimum pulse length with which cells can be deflected is particularly important, because the shorter the pulse length is, the higher the event rate can be. We determine the threshold length of the SAW pulse for a range of radio frequency (RF) power levels. As the RF power increases, pulses with shorter durations provide enough energy to deflect cells. Cells can be efficiently actuated provided the SAW pulses are at least 20 μs long, as shown in Fig. 3b. Because the device can successfully deflect cells with short bursts of acoustic waves, the length of the pulse does not limit the instrument's performance at high event rates.

Different cell types

Our sorting device also needs to be able to sort a variety of cell types. We use the same range of power levels and pulse lengths to test whether the device can sort adherent and non-adherent cell types. For adherent cell type, we chose MDCK cells which are approximately 8 μm in diameter.[35] For non-adherent cell type, we chose K562 cells which are approximately 15 μm in diameter.[36] Both classes of cells can be reproducibly deflected into the groove with similar SAW pulse parameters, also shown in Fig. 3b. However, the threshold power slightly differs between the cell types, due to small differences in the average size or acoustic contrast of the cells. Nevertheless, the slanted groove device can actuate both adherent and non-adherent cells with the short pulse lengths necessary to attain high screening rates.

Dependence on groove dimensions

The shape and orientation of the groove may also be tuned to improve sorting performance. We examine the impact of groove geometry on cell actuation in our design by varying the groove width, height, and angle independently. As the groove is widened, less power is necessary to cause the cell to interact with the flow within the groove, as demonstrated in Fig. 3c. While it is possible to sort cells without any groove or with a very shallow groove, the best sorting results are obtained with grooves fabricated at a height of 25 μm, as shown in Fig. 3d. This corresponds to the deepest groove that gives reliable results. Different groove angles show no significant effect on the threshold power required for sorting. While there may be slight variations due to changes in the effective aperture of the groove or in the flow speed along the groove, these effects are within the range of measurement error, and appear to have very little effect on the threshold power. Our results demonstrate that both the depth and the width of the groove provide geometrical tuning parameters, which can influence the interaction of cells with the groove when SAWs are applied.

Other operating limitations

Because the threshold power for each parameter is within the operating range of the device, we should be able to achieve sorting at high event rates; however, there are additional device limits to consider. In terms of the acoustic wave power, the SAW cannot push cells high enough to interact with the groove for power levels below 3 W. Increasing the power increases the success rate of sorting, but only until about 10 W, when we start to see IDT damage in the form of chip cracking. To increase the rate, we would also like to increase the total flow rate, but, in our device, for flow rates exceeding 60 ml h^{-1}, the cells are not effectively confined to a narrow thread, which prevents us from testing SAW actuation with higher cell velocities. There are also limits on the groove geometry. When the height and width of the groove are increased to 50 μm or 160 μm respectively, cells begin to enter the groove without any applied SAW, which is detrimental to the purity of the recovered cells. Having these limitations in mind the optimal condition of sorting and prevention of false positive in the sorting channel is a groove width in the range of 120–160 μm and a groove height of 25–50 μm. In all subsequent experiment we therefore choose a width of 120 μm and height of 25 μm to stay away from the boundaries where false positive occur. Despite these limitations, there are a wide range of conditions for which the slanted groove device provides stable and reliable operation.

Sorter performance

The extent to which we can achieve reliable operation with our sorting device can be measured by applying the sorting conditions we determined here to cell samples. For a given cell phase flow rate, a high cell density is required to reach a high event rate. However, this increases the chance of coincidence events. To measure the sorter's performance at different cell densities, we prepare a reference sample of K-562 cells in which the cell density and the fraction of fluorescent cells are known. The sorter extracts the fluorescent cells. The purified sample is collected and the recovered cells are imaged using a confocal microscope to obtain an independent measurement of cell purity. To elucidate how the purity of the sorted fraction depends on event rate, we increase the density of cells in the mixed sample, while keeping the cell phase flow rate constant. We also operate the device with two different sheath flow rates and two different groove widths, to measure how these parameters affect sorter performance. These experiments provide a realistic picture of how devices with slanted grooves will perform.

Purity

As expected, the sorter achieves high purity at low event rates, but the purity decreases, as the concentration of cells

increases with a trend that appears linear, as shown in Fig. 4a. The data fits to a line, which intersects the purity axis at 93% and whose slope represents a loss in purity of 4.3% each time the event rate increases by 1000 events per s. This y-intercept represents the theoretical maximum purity for the set of devices we tested. Although this fit describes the average performance of these sorting devices, we examine the distributions of the residuals for each parameter in more detail, to see if the operating flow rate or the slanted groove width influence device performance. For different sheath flow rates, there is no clear difference between the purity of the recovered samples. However, when we test different groove widths, we observe that the purity of samples isolated using devices with a 40 μm groove is higher than for devices with an 80 μm groove. This difference was statistically significant with a probability of only 0.28% indicating that these sets of residuals are drawn from the same distribution. Box plots showing the distributions of residuals grouped by applied flow rate and groove width are plotted in Fig. 4b and c respectively. Because the width of the slanted groove has a clear effect on device performance, we fit the data from different groove widths independently. The purity of samples recovered using the device with the 40 μm groove decreases 4.0% per 1000 events per s with a theoretical maximum at 95.7%, while

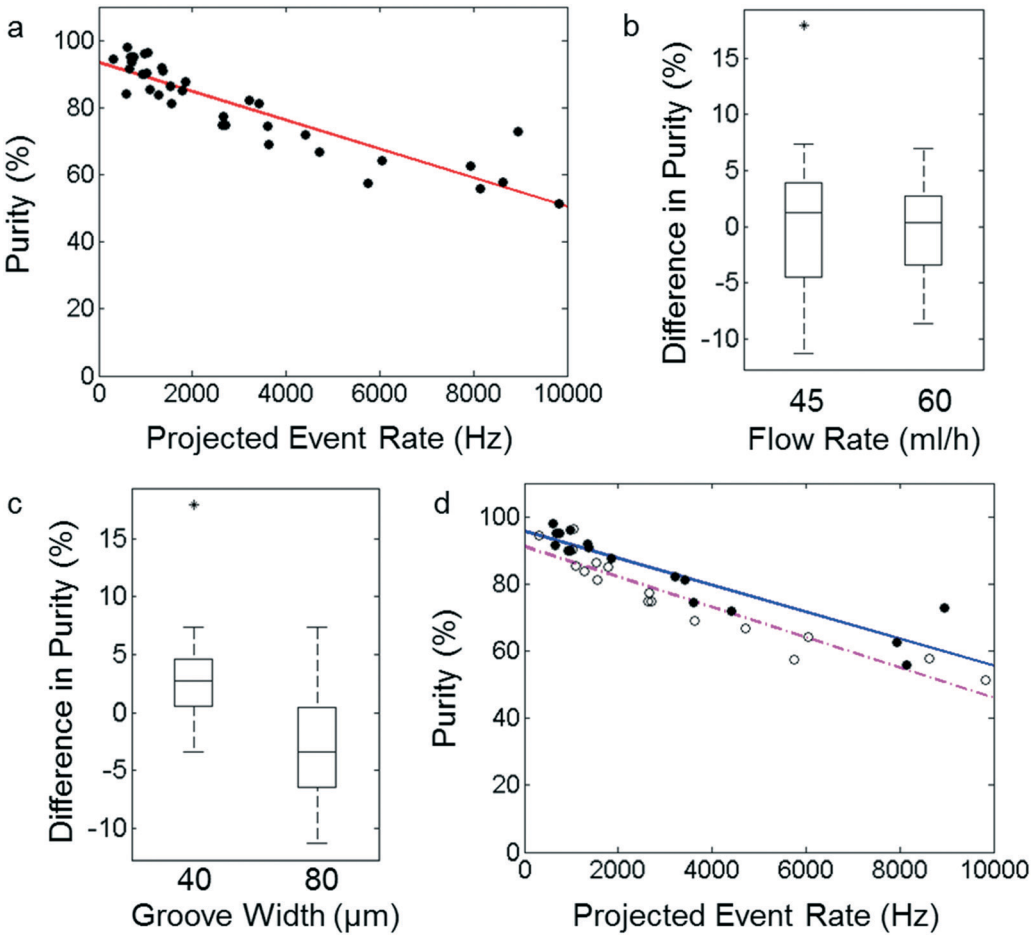

Fig. 4 Sorting performance of sorting devices with slanted grooves. The purity of each recovered sample is plotted relative to the event rate at which the sample is sorted. (a) All the data points follow the same general trend. The entire data set fits to a line whose slope indicates a decrease in purity of 4.3% each time the event rate increases by 1000 events per s and whose intercept indicates that the theoretical maximum purity of the sorter is 93% (R^2 = 0.817). We determine the residuals of the data with respect to this fit, and group them based on the total sheath flow rate that was applied in (b) and the slanted groove width in (c) for each experiment. The distributions of the residuals are plotted as box and whisker plots for each group. The horizontal lines contained within each of the boxes indicate the median values; the upper and lower edges of the boxes indicate the upper and lower quartiles respectively; and the whiskers show the full range of the data. Outliers are indicated using stars. When the data are grouped according to the total sheath flow rate, the difference between the two populations is not significant (p = 0.90). However, when the data are binned according to the width of the slanted groove, the devices with the narrower groove produce samples that are about 5% more pure than the devices with the larger groove, and there is a statistically significant difference (p = 0.0029) between the distributions for the 40 μm and 80 μm grooves. We further measure the effect of groove width on performance by fitting the data from the different groove widths independently. The data and the fits for the different groove widths are shown in (d). Filled circles (●) are used for samples sorted with a 40 μm groove device, while empty circles (○) represent samples sorted with the 80 μm groove. The device with the 40 μm groove has a slope of −4.0% per 1000 events per s and an intercept at 95.7% (R^2 = 0.849), while the device with the 80 μm groove has a slope of −4.5% per 1000 events per s and an intercept at 91.1% (R^2 = 0.879).

the purity of samples recovered from the device with the 80 μm groove decreases 4.5% per 1000 events per s and the fit intersects the purity axis at 91.1%, as shown in Fig. 4d. These results indicate that decreasing the width of the slanted groove in our sorting design provides a means of improving the purity of the sorted sample, for the whole range of event rates.

The observation that the device with a narrow groove yields higher purity suggests that the groove plays another role in the sorting process. Because cells that enter the groove are carried across the sorting channel to the sorting outlet, it must be more difficult for non-target cells to enter the narrow groove. We propose that the groove acts as a spatial filter; cells can only enter the groove, if they are aligned with the groove when the acoustic wave is applied. This effect offers a unique advantage compared to previous SAW sorting designs, in which the sorting purity can only be increased by changing the design of the SAW transducer or the operating flow rates. With the 40 μm groove, our design can achieve on average 92% purity at 1000 events per s; moreover, the device succeeds to enrich cells at event rates of nearly 10 000 events per s.

Although the purity appears low, our characterization experiments show that the slanted groove is capable to operate at high rates. In conventional FACS instruments, high levels of purity require detection and elimination of coincidence events. Our instrument could be improved by incorporating the hardware and software designed for FACS instruments. In addition, the nozzle used for vertical flow focusing is a relatively simple design. While it serves to illustrate the principle of operation of the device, it could be further optimized to increase the spacing between cells and to minimize the dispersion of cell velocities. Moreover, after sorting with the slanted groove device, the viability of the sorted fraction of cells remains high, greater than 96% based on membrane integrity. As a result, we believe that cell sorters based on traveling SAWs are already promising and will benefit from the fast pace of development in cell sorting using microfluidics and will soon be able to compete with FACS instruments.

Conclusions

Cell sorters with slanted grooves use traveling SAWs to sort cells rapidly to high levels of purity. The design features guide the vertically translated cells to isolate desired cells. The sorter operates at high rates, approaching those of commercial FACS instruments, and features a high purity mode for recovery of enriched samples. Like other microfluidic cell sorters, the fluid handling region is enclosed and aerosols are not produced by the acoustic waves in the system; therefore, the sorter could find application particularly in screening bio-hazardous samples without the need for additional containment measures.[1,14] Moreover, the same SAW device platform is compatible with both cells and droplets,[8] so a single instrument could provide users with both FACS and droplet sorting capabilities. The slanted groove devices demonstrated here could be further enhanced by integrating numerous recent advances in flow focusing,[37,38] inertial microfluidics,[14] and SAW microfluidics.[39] As a result, the SAW-actuated cell sorter with a slanted groove offers a promising alternative to both traditional FACS instruments and other microfluidic methods of sorting that could see widespread use.

Experimental

Device design

The device consists of a PDMS replica containing the device's flow channels bonded to a SAW substrate next to an IDT. Drawings of the IDT design and the microfluidic device are created using AutoCAD (Autodesk, Inc., San Rafael, CA). The structures defined in the drawings are transferred photomasks for lithography. These photomasks are used to fabricate molds for the PDMS replicas and to pattern metal onto each SAW substrate to form IDTs.

The IDT has a tapered or fanned design.[26] In the tapered design, the pitch of the IDT fingers varies laterally across the transducer. The pitch increases linearly with position between a smaller pitch on one side of the transducer and a larger pitch on the opposite side; therefore, the resonant frequency also varies with position along the transducer. In our IDT, the resonant frequency range is between 161 and 171 MHz.[39,40] We have chosen this comparatively high frequency since the effect of acoustic streaming increases with the square of the frequency. The width of the resonance region is determined by the full width of the IDT and the frequency difference between the two edges;[41] it is approximately 100 μm in our design. The metallization ratio is the fraction of the IDT in each finger repeat that is covered by metal; this ratio is kept constant at 0.5. Bus bars on either side of the IDT connect to square pads with 1.5 mm side length, through which external voltages are applied to all the IDT fingers with minimal resistance. Additional markings delimit each transducer so that the IDTs can be cut from the wafer into individual squares with 17.4 mm side length. The design is etched into a chrome mask (Photo-Sciences Inc., Torrance, CA) to ensure that the actual finger widths closely match the designed values.

The microfluidic device has three layers, each fabricated using a separate photomask. The first layer contains only the shallow channel that serves as the vertical flow-focusing nozzle. The pattern for the nozzle extends underneath both the cell inlet region and the sorting channel to ensure that the nozzle is not sensitive to the alignment of subsequent layers. The constriction in the nozzle is designed to be nominally 40 μm long, reducing the chance that cells will clog the nozzle. The sheath channels form a Y-shape with the sorting channel, so that no stagnation points are formed, as the flow emerges from the nozzle. The nozzle is offset from the centre of the channel, so that variations in flow rate or other unwanted perturbations will not cause cells to enter the retention channel spuriously. The bulk of the device's features

are on the second layer, including the sheath and cell inlets, the main flow channel, and the device outlets. In addition, the fingers of the IDT are situated beneath an air gap, to prevent the acoustic waves from leaking into the PDMS device. The thickness of the PDMS separating the air gap from the liquid in the channel is also minimized to reduce power loss. This air gap does also exist in the second device layer. The third layer only contains the slanted groove, which is patterned on top of the sorting region of the channel. The groove is drawn 230 μm wide, slightly less than the full sorting channel width, ensuring that even if the groove is slightly misaligned from the sorting channel, the wall of the channel where the acoustic wave encounters the liquid will not be distorted. Distortions of the channel wall cause the acoustic wave to refract at unexpected angles.[42] Each layer contains at least two sets of alignment marks consisting of an asymmetrical pattern of crosses,[43] enabling different layers to be aligned precisely on top of each other. The masks for the individual microfluidic device layers are ordered from CAD/Art Services, Inc. (Bandon, OR) and imaged with a resolution of 25 400 dpi.

Transducer fabrication

Interdigital transducers are fabricated using the lift-off process described in the protocol from the Center for Nanoscale Systems at Harvard University.[44] The substrates are 4 inch wafers of black lithium niobate (Precision Micro-Optics, LLC, Woburn, MA). Black lithium niobate is effective in SAW applications and exhibits less pyroelectric effect than undoped lithium niobate, making it convenient for lithographic processes that require baking at high temperature.[45] We choose 128° *Y–X* lithium niobate, because it has high SAW velocity and strong coupling.[26]

Each wafer is cleaned by spinning it at 4000 rpm, spraying it with acetone and isopropanol, and letting it continue to spin until dry. Residual moisture is removed with a dehydration bake at 180 °C for 1 minute. We ease the rate of temperature change by placing the wafer on a hot plate at 115 °C for 1 minute just prior to and immediately following baking at 180 °C. Resist is dispensed onto the wafer using a disposable dropper. A layer of LOR3A resist (MicroChem, Westborough, MA) is added to the wafer surface; then, the wafer is spun at 4000 rpm to create a layer 300 nm thick. We bake the resist at 180 °C for 4 minutes, using the same temperature ramping method as for the dehydration bake. We then add a layer of Shipley 1805 (MicroChem) and spin that at 4000 rpm. This layer is baked for 1 minute at 115 °C. The photoresist layers are exposed to UV light through the chrome mask with the IDT pattern on a contact mask aligner (MJB4, Karl Süss, Garching, Germany). We develop the pattern by immersing the wafer in CD-26 developer (Microposit, Austin, TX) for 75 s to form a shadow mask for E-beam deposition. We rinse the wafer clean with water and blow it dry with nitrogen. We clean the exposed surface of the wafer using an oxygen plasma cleaner (SCE106, Anatech, Union City, CA) with 75 W of RF power and an oxygen gas flow rate of 40 sccm for 20 s. We deposit 10 nm of titanium as an adhesion layer, followed by 50 nm of gold using electron beam physical vapor deposition (Denton Explorer 14, Denton Vacuum LLC, Moorestown, NJ) to form electrodes on the wafer. The photoresist is then lifted off by soaking the wafer in Remover-PG (MicroChem) at 80 °C until all the excess resist is removed, about 60 minutes. We add a layer of Shipley 1813, and bake it at 115 °C for 1 minute to form a protective layer. We use a dicing saw (DAD321, DISCO Corp., Tokyo, JPN) to score lines 250 μm into the lithium niobate. The wafer breaks cleanly along the scored lines, yielding up to 21 devices per wafer. The IDTs are cleaned with acetone to remove the protective layer, prior to use.

Soft lithography

We perform multi-layer lithography to create molds for PDMS replicas. The layers are processed following the method recommended in the manufacturer's data sheet for SU-8 3025 photoresist (MicroChem). For each layer, we dispense a small amount of resist onto the wafer. We spin the wafer at 3000 rpm to create a layer that is 25 μm thick. We pre-bake each layer for a total of 12 minutes at 95 °C, rotating the wafer 180° on the hot plate after half the bake time has elapsed. The photomask for a particular layer is aligned with any underlying features and the layers of photoresist are patterned with UV light on a contact mask aligner (ABM, Scotts Valley, CA). The resist is then post exposure baked for 1 minute at 65 °C and 5 minutes at 95 °C. At this point, additional layers can be added on top of any existing layers by following the same procedure. Once all the layers are post exposure baked, we develop the features by immersing the wafer in polyethylene glycol monomethyl ether acetate (484431, Sigma-Aldrich Co. LLC, St. Louis, MO) for 5 minutes using an orbital shaker (Roto Mix 8 × 8, Thermo Fisher, Waltham, MA) for mixing. After development, we rinse the wafer with isopropanol and blow it dry with nitrogen. We place the wafer in a 100 mm plastic petri dish. The wafer is now ready to serve as a mold for creating replicas in PDMS.

We mix PDMS (Sylgard 184, Dow-Corning, Midland, MI) base and cross-linker in a 10 : 1 weight ratio using a Thinky mixer (AR-100, Thinky Corp., Tokyo, Japan). The mixer runs in mixing mode for 30 s and degassing mode for another 30 s. We pour the uncured PDMS on top of the mold. We degas the PDMS for 10 minutes, then place the mold in the oven at 65 °C overnight. Once the PDMS is cured, we cut around the edge of the wafer using a scalpel and lift the PDMS replica out of the mold. Each PDMS replica contains 16 independent devices; the replica is cut into individual devices prior to use. Interface holes are created with a biopsy punch (Uni-Core, GE Healthcare Life Sciences, Pittsburgh, PA). We use 0.75 mm diameter holes for the inlets and 1.5 mm diameter holes for the outlets. We clean the replicas by sonication in isopropanol for 5 minutes, then blow them dry. At this point, individual PDMS devices can be bonded onto a substrate

with the IDT pattern in the instrument's sample holder for sorting experiments.

Sorter apparatus

The sorting apparatus is similar to that detailed in previous publications,[12,46] except that the microscope is custom built using modular optomechanics (Thorlabs Inc., Newton, NJ) instead of using a commercially available microscope. A 473 nm laser with 100 mW of output power (LRS-0473, Laserglow Technologies, Toronto, ON) excites fluorescence in the sample. The laser beam is expanded (BE-05-10-A, Thorlabs Inc.), and steered into the microscope. A cylindrical achromat (ACY254-200-A, Thorlabs Inc.) and a microscope objective (Nikon CFI Plan Apochromat Lambda, 10×/0.45NA, Micro Video Instruments, Inc., Avon, MA) focus the laser beam into a line in the microscope's focal plane. The objective also collects any fluorescence emitted by the sample. While excitation light gets reflected by the excitation dichroic (FF495-Di03-25 × 36, Semrock, Inc., Buffalo, NY) and up through the objective, the emitted fluorescence passes through the excitation dichroic. The fluorescence reflects off the fluorescence dichroic (FF605-Di01-25 × 36, Semrock, Inc.) towards the photocathode of a photomultiplier tube (H10723-20, Hamamatsu Photonics K.K., Hamamatsu, Japan). A colored glass longpass filter (FGL495, Thorlabs Inc.) and a dielectric bandpass filter (FF01-520/44-25, Semrock, Inc.) are placed between the fluorescence dichroic and the photomultiplier tube (PMT) to attenuate noise sources of light, so that the PMT provides an accurate measurement of fluorescence. The microscope's field of view is illuminated using an infrared light emitting diode (M780 L2-C1, Thorlabs Inc.). The infrared light passes through both microscope's dichroic filters, and gets reflected by a turning mirror (CM1-P01, Thorlabs Inc.). The infrared image is focused onto the sensor of a fast camera (HiSpec1, Fastec Imaging, San Diego, CA) by a tube lens (AC254-100-B-ML, Thorlabs Inc.). The fast camera enables the system to record high framerate videos of the sorting process. A manual stage (Leica) provides fine adjustment of the sample position with respect to the optical system.

The photomultiplier tube module measures the fluorescence from the sample, generating a voltage proportional to the intensity of the incident light. This voltage is digitized by the data acquisition card (PCIe-7842R, National Instruments Corp., Austin, TX) and analyzed in real time using the card's field programmable gate array to detect and analyze peaks in the fluorescence signal. When peaks corresponding to desired cells are detected, a sorting pulse is generated. The sorting pulse is a +3.3 V signal, which controls the output of a RF waveform generator (SMB100A, Rohde & Schwarz, Munich, Germany) through its pulse modulation input. The output of the waveform generator is intensified using a high gain RF amplifier (LZY-22+, Mini-Circuits, Brooklyn, NY). When the amplified RF signal is applied to the IDT, the IDT generates SAWs in response. An associated PC can be used to set threshold values for peak detection and sorting and to monitor system performance. Using this system, the fluorescence from cells passing through the sorting region of the device is analyzed in real time, and pulses of SAW are applied to sort desired cells with minimal latency.

A custom-made sample holder supports the microfluidic device. The base plate of the sample holder holds the IDT securely in a milled slot. The center of the baseplate is cut away to enable light to transmit through the sample and to permit the microscope to focus on the device. A glass slide is cut to size and placed under the IDT to provide mechanical support. A clear piece of lithium niobate is fastened underneath the glass slide in an orientation chosen to cancel the effects of substrate birefringence. A printed circuit board (PCB) routes signals from the amplifier to the IDT. The amplifier and the PCB are connected using standard RF adaptors (SMA to MMCX male), and electrical connections from the PCB to the IDT are created, when pogo pins mounted on the board are pressed into contact with the metal pads. The PCB is held in place by fixing it to the base plate using M3 screws. An acrylic spacer ensures that the pins exert enough force to hold the IDT in place and make consistent electrical contact, but not so much force that the substrate cracks under the stress. The spacer is milled to 3.7 mm and laser cut to accommodate the mounting screws, the shape of the PCB, and any electrical components on the lower side of the PCB. Each PDMS device is bonded to the substrate using mechanical force. The PDMS device forms three sides of the device's flow channel, while the lithium niobate substrate serves as the bottom of the flow channel. A clamp is fashioned from a 6 mm thick sheet of acrylic; it is laser cut to permit fluid connections to pass through to the PDMS device. The clamp presses the PDMS device onto the substrate using M2 screws fastened to the baseplate. Once assembled, the entire sample holder fits into the microscope stage.

Device characterization experiments

Madin Darby canine kidney (MDCK) and human chronic myelogenous leukemia (K-562, ATCC, Manassas, VA) cells are harvested prior to each day's experiments. The MDCKs have fluorescent nuclei, following stable transfection with green fluorescent protein fused to a nuclear localization sequence, while the K-562 cells are stained by adding calcein AM (Life Technologies, Grand Island, NY) to the cell suspension at a concentration of 1 μM and incubating the suspension at 37 °C for 20 minutes. The cells are re-suspended into injection buffer at between 5 and 10 million cells per ml. Injection buffer consists of 18% Optiprep (D1556, Sigma-Aldrich Co. LLC) by volume, 6 U ml^{-1} DNAse I (New England Biolabs Inc., Ipwich, MA), and 3 mM magnesium chloride in 1× phosphate buffered saline (PBS, P3813, Sigma-Aldrich Co. LLC, St. Louis, MO).

Unless otherwise specified, we use a PDMS device with a vertical flow-focusing nozzle that is 50 μm wide, 40 μm long and 25 μm tall; a sorting channel that is 250 μm wide and

50 μm tall; and a slanted groove that is 120 μm wide, 25 μm tall, and whose long axis is tilted 60° from the overall direction of flow. The flow rate of the cell phase is 0.5 ml h^{-1}, while the sheath fluid has a flow rate of 45 ml h^{-1}. The sheath fluid is 1X PBS. One quarter of the sheath flow comes from the inlet nearest the waste outlet and three quarters of the flow from the inlet on the retention side of the device.

The frequency of the RF pulse used to generate SAWs is kept constant at 163.1 MHz, except when the groove width is changed, then we tune the frequency to ensure that the SAW aligns with the groove. For each distinct condition, we run control experiments to ensure that cells are not sorted, when the instrument is triggered, but the RF source is off. Unless noted, no cells enter the retention channel unexpectedly for the conditions we tested. Fast movies of individual sorting events are analyzed to determine whether the cell is successfully deflected into the retention outlet or not.

Sorting experiments

As detailed for the characterization experiments, K-562 cells are harvested from culture just prior to conducting the experiment. To create reference libraries of cells, we mix the sample of cells carefully with a pipette and collect 10% of the cell suspension by volume. This fraction of the cells is stained with calcein AM at 1 μM for 20 minutes at 37 °C, while the remaining cells are kept unstained. The two fractions are then combined and the cells are re-suspended in injection buffer at the target cell density.

The cells are sorted using a slanted groove sorting device. We use the standard nozzle geometry and an RF pulse with 38.26 dBm of instantaneous power and 100 μs duration at 164.1 MHz. The flow rate of the cell suspension is kept constant at 0.5 ml h^{-1}. The device is operated with a range of cell densities to test different event rates. We measure the purity from devices operating at two different sheath flow rates, 45 ml h^{-1} and 60 ml h^{-1}, and using two different groove widths, 40 μm and 80 μm. The remaining control parameters are kept are held constant. Here, the sheath flow is 1× PBS. The actual rate of fluorescent events is measured by the sorting instrument and the projected total event rate is obtained by dividing this by the measured purity of the initial reference library. We set the thresholds for sorting to ensure that pulses are only applied when we expect only a single fluorescent cell to be present in the channel, by ignoring the lower and upper extremes of fluorescence. In addition, when the sorting rate is high, we further limit the sorting thresholds to set the sorting rate below 500 events per s, reducing the chance that the IDT will be irreversibly damaged. The fluorescence of the cells recovered from the retention outlet is measured using a confocal microscope (SP5, Leica Microsystems Inc., Buffalo Grove, IL). In addition to using calcein to measure the proportion of labelled cells in the recovered sample, DRAQ5 (Life Technologies, Grand Island, NY) is added at a final concentration of 500 nM to label the DNA of all cells present in each sample. To measure cell viability after sorting, we add ethidium homodimer (Life Technologies, Grand Island, NY) to 2 μM final concentration and incubate the cells with the dye for 20 minutes at 37 °C. The images are analyzed using a custom Matlab (The Mathworks, Inc., Natick, MA) script to detect fluorescence in the three separate fluorescence channels. The purity of the sorted fraction is the ratio of cells labeled with calcein to the total number of cells, and the viability is the difference between unity and the ratio of dead cells to total cells.

Conflicts of interest

There are no conflicts to declare.

Acknowledgements

This work was supported by the National Science Foundation (DMR-1310266), the Harvard Materials Research Science and Engineering Center (DMR-1420570), and the Defense Advanced Research Projects Agency (HR0011-11-C-0093). This work was performed in part at the Center for Nanoscale Systems (CNS), a member of the National Nanotechnology Infrastructure Network (NNIN), which is supported by the National Science Foundation under NSF award no. ECS-0335765. CNS is part of Harvard University. TF acknowledges support by the DFG and the Bayerisches Staatsministerium für Umwelt und Verbraucherschutz, Germany. The authors would also like to thank Adrian Pegoraro and John Heyman for providing samples of MDCK GFP-NLS and K-562 cells respectively. WLU would especially like to thank Don Aubrecht, Tom Kodger, and Adrian Pegoraro for advice, assistance, and helpful discussions.

References

1 H. M. Shapiro, *Practical Flow Cytometry*, John Wiley & Sons, Inc., 4th edn., 2003.
2 A. H. R. Hulett, W. A. Bonner, J. Barrett and L. A. Herzenberg, *Science*, 1969, **166**, 747–749.
3 M. M. Wang, E. Tu, D. E. Raymond, J. M. Yang, H. Zhang, N. Hagen, B. Dees, E. M. Mercer, A. H. Forster, I. Kariv, P. J. Marchand and W. F. Butler, *Nat. Biotechnol.*, 2005, **23**, 83–87.
4 J. T. Merrill, *Cytometry*, 1981, **1**, 342–345.
5 M. Eisenstein, *Nature*, 2006, **441**, 1179–1185.
6 G. M. Whitesides, *Nature*, 2006, **442**, 368–373.
7 T. M. Squires and S. R. Quake, *Rev. Mod. Phys.*, 2005, **77**, 977–1026.
8 L. Schmid, D. A. Weitz and T. Franke, *Lab Chip*, 2014, **14**, 3710–3718.
9 Y. Chen, T.-H. Wu, Y.-C. Kung, M. A. Teitell and P.-Y. Chiou, *Analyst*, 2013, **138**, 7308–7315.
10 J.-C. Baret, O. J. Miller, V. Taly, M. Ryckelynck, A. El-Harrak, L. Frenz, C. Rick, M. L. Samuels, J. B. Hutchison, J. J. Agresti, D. R. Link, D. A. Weitz and A. D. Griffiths, *Lab Chip*, 2009, **9**, 1850–1858.
11 S. H. Cho, C. H. Chen, F. S. Tsai, J. M. Godin and Y.-H. Lo, *Lab Chip*, 2010, **10**, 1567–1573.

12 J. J. Agresti, E. Antipov, A. R. Abate, K. Ahn, A. C. Rowat, J.-C. Baret, M. Marquez, A. M. Klibanov, A. D. Griffiths and D. A. Weitz, *Proc. Natl. Acad. Sci. U. S. A.*, 2010, **107**, 4004–4009.
13 A. Sciambi and A. R. Abate, *Lab Chip*, 2015, **15**, 47–51.
14 Y. Chen, A. J. Chung, T. H. Wu, M. A. Teitell, D. Di Carlo and P. Y. Chiou, *Small*, 2014, **10**, 1746–1751.
15 A. A. Nawaz, Y. Chen, N. Nama, R. H. Nissly, L. Ren, A. Ozcelik, L. Wang, J. P. McCoy, S. J. Levine and T. J. Huang, *Anal. Chem.*, 2015, 150902104705000.
16 L. Ren, Y. Chen, P. Li, Z. Mao, P.-H. Huang, J. Rufo, F. Guo, L. Wang, J. P. McCoy, S. J. Levine and T. J. Huang, *Lab Chip*, 2015, **15**, 3870–3879.
17 J. Friend and L. Y. Yeo, *Rev. Mod. Phys.*, 2011, **83**, 647–704.
18 J. Shi, X. Mao, D. Ahmed, A. Colletti and T. J. Huang, *Lab Chip*, 2008, **8**, 221–223.
19 J. Shi, H. Huang, Z. Stratton, Y. Huang and T. J. Huang, *Lab Chip*, 2009, **9**, 3354–3359.
20 J. Shi, S. Yazdi, S.-C. S. Lin, X. Ding, I.-K. Chiang, K. Sharp and T. J. Huang, *Lab Chip*, 2011, **11**, 2319–2324.
21 X. Ding, S.-C. S. Lin, B. Kiraly, H. Yue, S. Li, I.-K. Chiang, J. Shi, S. J. Benkovic and T. J. Huang, *Proc. Natl. Acad. Sci. U. S. A.*, 2012, **109**, 11105–11109.
22 T. Franke, S. Braunmüller, L. Schmid, A. Wixforth and D. A. Weitz, *Lab Chip*, 2010, **10**, 789–794.
23 X. Ding, P. Li, S.-C. S. Lin, Z. S. Stratton, N. Nama, F. Guo, D. Slotcavage, X. Mao, J. Shi, F. Costanzo and T. J. Huang, *Lab Chip*, 2013, **13**, 3626–3649.
24 L. Y. Yeo and J. R. Friend, *Biomicrofluidics*, 2009, **3**, 1–23.
25 G. Destgeer, K. H. Lee, J. H. Jung, A. Alazzam and H. J. Sung, *Lab Chip*, 2013, **13**, 4210.
26 D. Morgan, *Surface Acoustic Wave Filters*, Elsevier Ltd., 2007.
27 D. J. Collins, T. Alan and A. Neild, *Appl. Phys. Lett.*, 2014, **105**, 193507.
28 Z. Mao, Y. Xie, F. Guo, L. Ren, P. Huang, Y. Chen, J. Rufo, F. Costanzo and T. J. Huang, *Lab Chip*, 2016, 515–524.
29 I. Leibacher, S. Schatzer and J. Dual, *Lab Chip*, 2014, **14**, 463–470.
30 R. W. Rambach, V. Skowronek and T. Franke, *RSC Adv.*, 2014, **4**, 60534–60542.
31 C. Devendran, D. J. Collins, Y. Ai and A. Neild, *Phys. Rev. Lett.*, 2017, **118**(118), 154501.
32 R. W. Ramback, J. Taiber, C. M. L. Scheck, C. Meyer, J. Reboud, J. M. Cooper and T. Franke, *Sci. Rep.*, 2016, **6**, 21980.
33 S. Chung, S. J. Park, J. K. Kim, C. Chung, D. C. Han and J. K. Chang, *Microsyst. Technol.*, 2003, **9**, 525–533.
34 C.-H. Hsu, D. Di Carlo, C. Chen, D. Irimia and M. Toner, *Lab Chip*, 2008, **8**, 2128–2134.
35 J. C. W. Richardson, V. Scalera and N. L. Simmons, *Biochim. Biophys. Acta*, 1981, **673**, 26–36.
36 G. Wang, C. Turbyfield, K. Crawford, A. Alexeev and T. Sulchek, *Microfluid. Nanofluid.*, 2015, **19**, 987–993.
37 X. Mao, J. R. Waldeisen and T. J. Huang, *Lab Chip*, 2007, **7**, 1260–1262.
38 A. A. Nawaz, X. Zhang, X. Mao, J. Rufo, S.-C. S. Lin, F. Guo, Y. Zhao, M. Lapsley, P. Li, J. P. McCoy, S. J. Levine and T. J. Huang, *Lab Chip*, 2014, **14**, 415–423.
39 R. W. Rambach, V. Skowronek and T. Franke, *RSC Adv.*, 2014, **4**, 60534–60542.
40 L. Schmid and T. Franke, *Lab Chip*, 2013, **13**, 1691–1694.
41 X. Ding, J. Shi, S.-C. S. Lin, S. Yazdi, B. Kiraly and T. J. Huang, *Lab Chip*, 2012, **12**, 2491.
42 I. Leibacher, P. Hahn and J. Dual, *Microfluid. Nanofluid.*, 2015, **19**, 923–933.
43 *Stanford Microfluid. Foundry*, 2015.
44 S. Hickman, *Harvard Center for Nanoscale Systems*, 2011, 1–10.
45 E. M. Standifer, D. H. Jundt, R. G. Norwood and P. F. Bordui, *Ieee Int. Freq. Control Symp.*, 1998, 470–472.
46 L. Mazutis, J. Gilbert, W. L. Ung, D. A. Weitz, A. D. Griffiths and J. A. Heyman, *Nat. Protoc.*, 2013, **8**, 870–891.